

Active Millimeter Wave Imaging Using Leaky-Wave Focusing Antenna

Kevin Kipruto Mutai^{id}, Graduate Student Member, IEEE, Hiroyasu Sato, Member, IEEE, and Qiang Chen^{id}, Senior Member, IEEE

Abstract—In this article, an active millimeter-wave imaging system using two rectangular waveguide leaky-wave focusing antennas deployed in a quasi-monostatic transmitter and receiver pair is proposed. The broadband design method of the focusing antenna is presented, where the phase constant is derived from the radiation direction of a rectangular waveguide leaky-wave antenna. To eliminate the effect of mutual coupling between the transmitting and receiving antennas and scattering from the surrounding environment, the scattered field from the object is obtained by subtracting the incident field from the total field. The 1-D detection of conducting sphere, conducting and dielectric cylinders, and a conducting plate is performed by experiment to validate the imaging capability of the proposed system. The 2-D imaging of a conducting cylinder in free space and positioned in front of a human body phantom representing the human body is finally performed to simulate the practical application of the system.

Index Terms—Antenna synthesis, focusing, leaky-wave antennas (LWAs), millimeter-wave (MMW) imaging, MMW radar.

I. INTRODUCTION

DUE to the increasing threat of terrorism and criminal activities globally, surveillance at security checkpoints, such as airports and sports stadia, is becoming increasingly important. Current personnel scanning technologies that include metal detectors and X-rays have disadvantages where metal detectors are only effective against metal objects, whereas X-ray has some perceived harmful health effects. To address these problems, millimeter-wave (MMW) imaging technologies have been developed that offer advantages such as accuracy in low visibility conditions and the ability to penetrate clothing and detect both conductors and dielectrics without harmful health effects [1]–[6].

Current MMW imaging systems, however, have some disadvantages associated with them. One disadvantage is that they require a 2-D array of sensors, which increases the fabrication

costs [7]–[9]. The 2-D array of sensors was reduced to a 1-D array by using a flapping reflector in [10]; however, a large dielectric lens was required for focusing, which increases the overall size of the system [10], [11]. This limits portability, which means that some hard-to-reach target areas may not be scanned. To eliminate the need for an array of sensors, an alternative method would be to use the frequency scanning characteristic of a leaky-wave antenna (LWA) to scan across a target scene by changing the frequency. In addition, if the LWA structure is of an appropriate physical profile, then a handheld MMW imaging system based on the LWA is a possibility and is the target of this study.

The LWA is a type of traveling wave antenna where the radiation direction changes as the frequency is changed [12], [13]. If focusing can be achieved using the LWA and, thereby, eliminate the need for a dielectric lens or metal reflector, then the LWA would have potentially useful imaging applications. Focusing type LWAs have been proposed in [14]–[17]. However, due to the need for handheld operation, a waveguide focusing LWA is a convenient option due to the relatively more portable physical profile of these antennas.

In this article, we propose an active MMW imaging system using two of the leaky-wave focusing antenna (LWFA) first proposed by our group in [18]. The LWFA is based on a tapered rectangular waveguide structure where focusing is achieved in the near field by changing the height of the broad wall of the waveguide. Due to the leaky-wave nature of the LWFA, one advantage is that the focusing position changes with frequency, which allows the scanning of multiple positions along one direction simply by changing the frequency, and this concept is shown in Figs. 1 and 2.

Another feature of the LWFA is the cutoff effect that appears due to the changing h along the length of the antenna. However, instead of being a disadvantage, the cutoff effect is used to control the amplitude distribution across the frequency range of operation such that an amplitude distribution centered about the center frequency is obtained and approximates a uniform amplitude distribution.

The LWFA is discussed in Section II. The proposed imaging system is discussed in Section III. Simulation and experimental results are presented and discussed in Section IV.

II. DESIGN OF LEAKY-WAVE FOCUSING ANTENNA

Tapering of the broad wall height in a rectangular waveguide LWA to obtain focusing in the near field was first explored

Manuscript received June 8, 2021; revised October 7, 2021; accepted November 20, 2021. Date of publication December 29, 2021; date of current version May 5, 2022. This work was supported in part by the Japan Society for the Promotion of Science (JSPS) KAKENHI under Grant 20K04515 and in part by the Ministry of Internal Affairs and Communications in Japan under Grant JPJ000254. (Corresponding author: Kevin Kipruto Mutai.)

The authors are with the Department of Communications Engineering, Graduate School of Engineering, Tohoku University, Sendai 980-8579, Japan (e-mail: mutai-k@ecei.tohoku.ac.jp; sahiro@ecei.tohoku.ac.jp; chenq@ecei.tohoku.ac.jp).

Color versions of one or more figures in this article are available at <https://doi.org/10.1109/TAP.2021.3137533>.

Digital Object Identifier 10.1109/TAP.2021.3137533

0018-926X © 2021 IEEE. Personal use is permitted, but republication/redistribution requires IEEE permission. See <https://www.ieee.org/publications/rights/index.html> for more information.

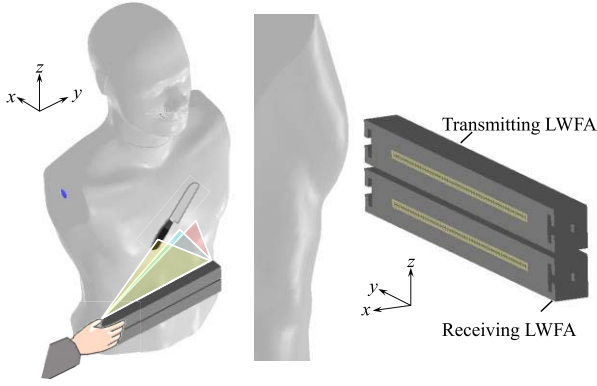


Fig. 1. Proposed imaging scenario.

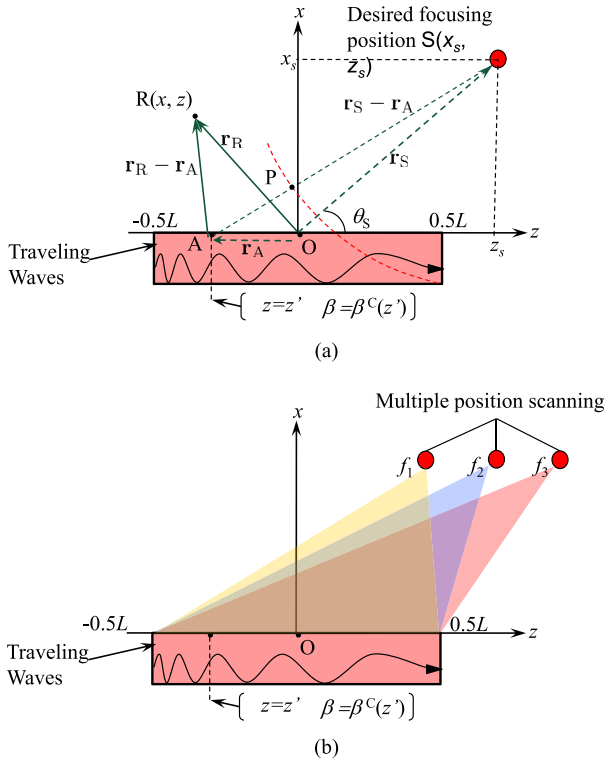


Fig. 2. Concept of (a) LWFA and (b) multiple position scanning by frequency sweep.

by our group in [18]–[20]. The theoretical background of the LWFA is based on the tapering of the leaky mode [21], where the phase constant β is varied along the longitudinal axis of an LWA. The variation is designed such that the field contributions along this length add in phase at the desired focusing position $S(x_s, z_s)$ in the near field (see Fig. 2) at a given design frequency.

The distance from an arbitrary position A on the surface of the LWFA of length L ($-0.5L \leq z' \leq 0.5L$) to the focusing position S is denoted as $|\mathbf{r}_S - \mathbf{r}_A|$. The distance from the center of the LWFA to S is denoted as $|\mathbf{r}_S|$, whereas the distance from A to a point P in the xz plane along $|\mathbf{r}_S - \mathbf{r}_A|$ is given as $|\mathbf{r}_S - \mathbf{r}_A| - |\mathbf{r}_S|$. If O is taken as the reference position, then the phase difference in the near field is given by

$$\Delta\Psi_P(z') = k_0(|\mathbf{r}_S - \mathbf{r}_A| - |\mathbf{r}_S|) \quad (1)$$

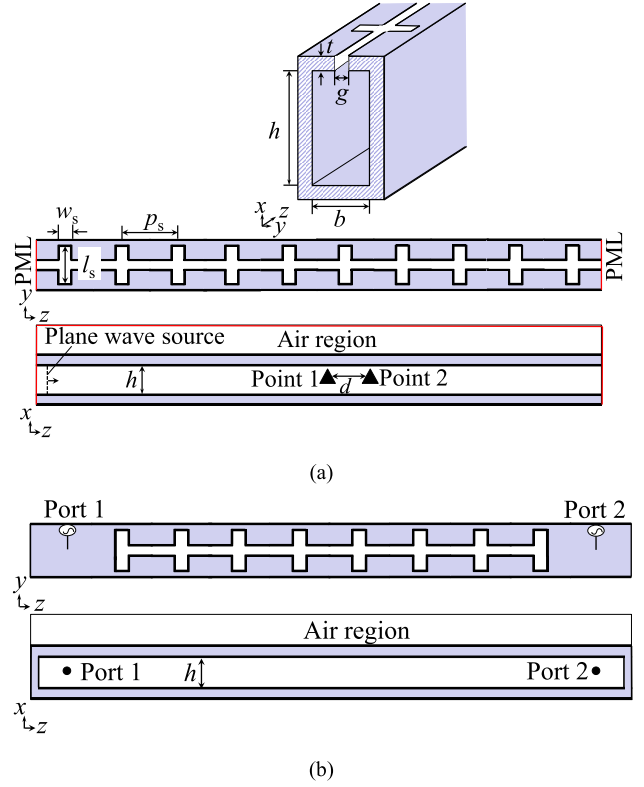


Fig. 3. FDTD analysis models of rectangular waveguide LWA with uniform broad wall height h used to obtain phase constant. Model (a) is used with (6), and (b) is used with (7). Parameters used are $t = 1$ mm, h was changed from 5.5 to 8 mm in increments of 0.5 mm, $b = 4$ mm, $w_s = 1$ mm, $g = 1$ mm, $p_s = 3$ mm, and $l_s = 2$ mm.

where

$$|\mathbf{r}_S - \mathbf{r}_A| - |\mathbf{r}_S| = \sqrt{(z_s - z')^2 + x_s^2} - \sqrt{z_s^2 + x_s^2} \quad (2)$$

and the phase distribution along the LWA is [22]

$$\beta(z') = \frac{d}{dz'} \Delta\Psi_P(z') \quad (3)$$

$$= k_0 \frac{z_s - z'}{\sqrt{(z_s - z')^2 + x_s^2}}. \quad (4)$$

$\beta(z')$ is used to obtain the focusing effect and is independent of the antenna structure.

The design frequency was selected as the center frequency, f_c , of 27 GHz. Equation (4) then takes the form

$$\beta^c(z') = k_0^c \frac{z_s - z'}{\sqrt{(z_s - z')^2 + x_s^2}} \quad (5)$$

where k_0^c is the wavenumber in free space at the center frequency. The height of the broad wall, h , is tapered along the length of the LWFA to realize (5). To obtain the required broad wall height distribution $h(z')$, the phase constant β of a rectangular waveguide LWA operating in the TE_{10} mode can be obtained by FDTD [23], [24] analysis at different values of h , and the equation relating h and β can then be derived.

A model of the LWA was designed in commercial full-wave simulation software and is shown in Fig. 3(a). The shorter

transverse slot parameters along the longitudinal slot were selected to suppress the slot mode from radiating [25]. The y -component of the electric field was extracted at two points located at z_1 and z_2 along the z -direction with distance d between them at the center of the waveguide for different h , as shown in Fig. 3(a). A z -directed plane wave source was used to excite TE₁₀ mode inside the model at 27 GHz. Perfectly matched layers (PMLs) were used to terminate the model at both ends to simulate a traveling wave and eliminate reflections inside the waveguide. The leaky mode complex wavenumber was then obtained by the following equation [24]:

$$k = \frac{1}{d} \left\{ \text{Arg} \left(\frac{E_y(z_1)}{E_y(z_2)} \right) - j \log \left| \frac{E_y(z_1)}{E_y(z_2)} \right| \right\}. \quad (6)$$

The real part of (6) corresponds to β' , while the imaginary part corresponds to the attenuation constant α' . Because $h(z')$ of the rectangular waveguide structure is varied, naturally, the cutoff effect appears for frequencies less than the cutoff frequency at each z' , which can be calculated by $f_{\text{cutoff}} = c_0/2h(z')$, where c_0 is the speed of light in free space. The attenuation constant corresponding to the cutoff effect, α_{CUTOFF} , is significantly higher than the attenuation constant due to leakage, α_{LWA} , in the LWFA [22] and is the main component in α' . It is because of this that L was selected with the resolution in mind, as discussed in Section IV, and not α_{LWA} even though the choice of L would also influence α_{LWA} . Both the slot mode and the leaky mode are contained in the result of (6), as discussed in [22], due to the propagation of the slot mode inside the waveguide. The radiation direction θ_S was, therefore, obtained for each h from observing the maximum gain in the model shown in Fig. 3(b) because the slot-mode is suppressed from radiating, and therefore, only the leaky-mode is expected to radiate. The resulting phase constant, denoted as β , was obtained using

$$\frac{\beta}{k_0} = \cos(\theta_S) \quad (7)$$

and is shown in Fig. 4.

The dispersion diagram comparing β' and β is shown in Fig. 4. The phase constant of a closed hollow rectangular waveguide, β_{WG} , is used only as a reference. β was extracted at 27 GHz for each value of h and denoted as β^C . The relationship between h and β^C/k_0 was derived by a fitted curve.

A fitted curve is needed because of the difficulty in determining δ accurately for each frequency and h . The fitted equation was obtained as

$$h(z') = 3.7122 \left(\frac{\beta^C(z')}{k_0} \right)^2 + 0.8453 \left(\frac{\beta^C(z')}{k_0} \right) + 5.3747. \quad (8)$$

The required $h(z')$ and $\beta(z')/k_0$ to obtain focusing at $S(x_s, z_s) = (195, 150)$ mm are shown in Fig. 5 for 27 GHz. To obtain the relationship between β/k_0 and h for other frequencies, a fitted curve can be obtained from Fig. 4. $h(z')$ in (8) can then be inserted into the resulting equation to find the $\beta(z')$ along the length of the LWFA at a given frequency. Because of the changing h , the propagating length, L_{act} , of the LWFA is limited for frequencies in the cutoff region. To find

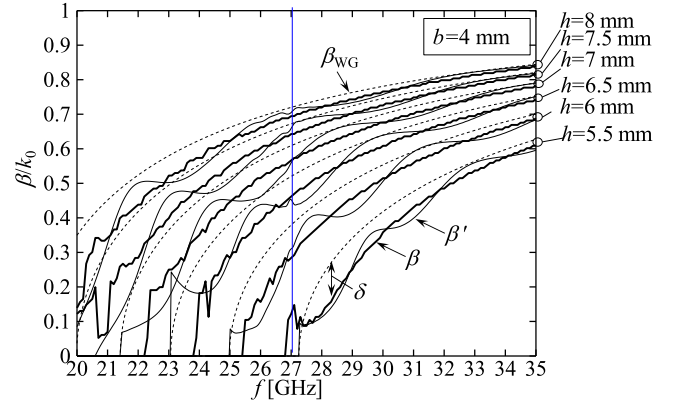


Fig. 4. Calculated frequency characteristics of phase constant for different h 's. β' is obtained from (6), using a field extracted from the inside waveguide, and β is obtained from (7), using the radiation direction of leaky waves. β_{WG} is the phase constant of the closed hollow rectangular waveguide and is used as a reference.

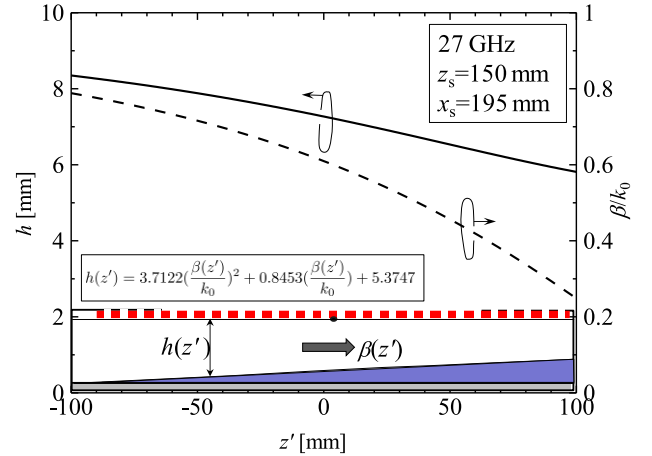


Fig. 5. Tapered height distribution and desired phase constant to obtain focusing at $S(x_s, z_s) = (195, 150)$ mm obtained using (5) at the center frequency of 27 GHz.

$L_{\text{act}}\beta$ is set to zero in order to find the h at which cutoff is first observed, denoted as h_{cutoff} . The position of this h_{cutoff} along the length of the LWFA, denoted as z_{act} , can be checked from Fig. 5. L_{act} can then be obtained by

$$L_{\text{act}} = \frac{L}{2} + z_{\text{act}}. \quad (9)$$

The minimum cutoff frequency for the LWFA is, therefore, about 18.7 GHz corresponding to $h_{\text{cutoff}} = 8.34$ mm at the position $z' = -100$ mm.

The LWFA structure is shown in Fig. 6, and the details on the parameters are presented in Table I. The fabricated prototype is shown in Fig. 7. The original prototype was manufactured using aluminum, and the weight was about 515 g excluding the coaxial to waveguide adapter. To further reduce the weight of the prototype, the waveguide component of the LWFA was then manufactured using acrylic material and is shown in Fig. 7, and the resulting structure was electroplated with a 10 μm -thick copper layer and a 1 μm nickel layer. As the skin depth of copper with $\sigma = 58.13$ MS/m at 27 GHz

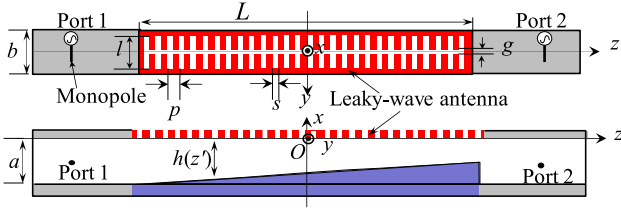
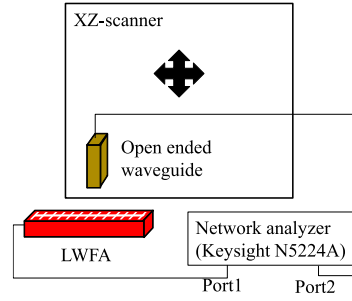
Fig. 6. Structure of LWFA with tapered h .

Fig. 8. Experiment setup to measure electric field distribution.

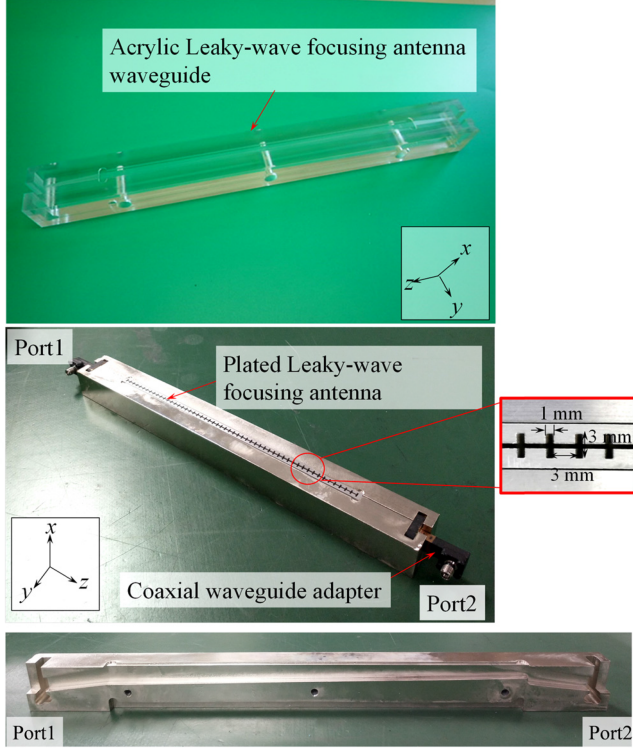


Fig. 7. Top view and side view of cross section of the fabricated LWFA prototype.

TABLE I
LWFA STRUCTURE PARAMETERS

Symbol	Quantity	Value
f	design frequency	27 GHz
L	length of antenna	200 mm
a	height of broad wall	8.2 mm
h	height of broad wall	Inhomogeneous
b	width of narrow wall	4 mm
p_s	pitch of slot	3 mm
l_s	length of slot	2 mm
w_s	width of slot	1 mm
g	width of slit	1 mm

is $\delta = (2/\omega\mu_0\sigma)^{1/2} = 0.4017 \mu\text{m}$, which is significantly lower than the thickness of the copper layer, the performance of the plated prototype is anticipated to be the same as that of the original solid aluminum prototype. The weight of the final plated structure, excluding the coaxial to waveguide adapter, is 230 g, which is less than half that of the original.

III. PROPOSED IMAGING SYSTEM

A. Conversion From Frequency Domain to Spatial z -Domain

The proposed imaging system was first presented in [26], whereby, using the frequency scanning capability of the LWFA, the image data collected will be in the frequency domain. To determine the object position and size from the image, it is necessary to convert the data from the frequency domain to the spatial domain. To this end, the experimental setup shown in Fig. 8 was used to measure the electric field distribution along the z -direction in the range $0 \text{ mm} \leq z \leq 300 \text{ mm}$ at $x = x_s = 195 \text{ mm}$ for different frequencies. An open-ended waveguide (OEWG) was moved along the z -direction at $x = x_s = 195 \text{ mm}$ in 5 mm increments, and the S-parameter between the OEWG and the LWFA was measured at each position. The peaks at each frequency were obtained and are shown in Fig. 9, and the peak positions along the z -direction at each frequency f were then denoted as z_{peak} . The figure shows the peaks measured in the case of the original aluminum prototype and the plated prototype. The peak levels and positions are almost the same in both cases, which means that the plated prototype offers similar performance to the original prototype. The relationship between z_{peak} in mm and f in GHz was then obtained by a fitted curve as

$$z_{\text{peak}}[\text{mm}] = -0.617f^2[\text{GHz}] + 51.5f[\text{GHz}] - 787. \quad (10)$$

Using (10), it is possible to convert the image data from the measured frequency domain to the spatial domain.

B. Imaging System Setup and Subtraction of Incident Field

The proposed imaging scenario is in a bistatic setup shown in Fig. 10, where the transmitting and receiving antennas' feed ports are separated to reduce the mutual coupling between the LWFAs. The transmitting antenna LWFA 1 has ports 1 and 2, whereas the receiving antenna LWFA 2 has ports 3 and 4. 50 Ω impedances terminated both Ports 2 and 4. The TE_{10} mode is excited at Port 1, and the scattering object positioned at $T(x_{\text{obj}}, z_{\text{obj}})$ is illuminated. The magnitude of the scattered wave due to the object was obtained by measuring the S-parameter between Ports 1 and 3 denoted as S_{31} . The weight of both LWFAs making up the imaging system, including the coaxial to waveguide adapters, is 527 g, which is about the same as conventional handheld metal detectors that weigh up to around 600 g.

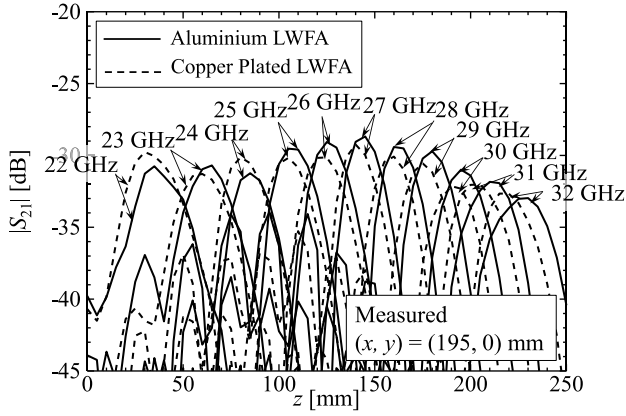


Fig. 9. Measured electric field distribution along the z -direction at $x = 195$ mm for 22–32 GHz.

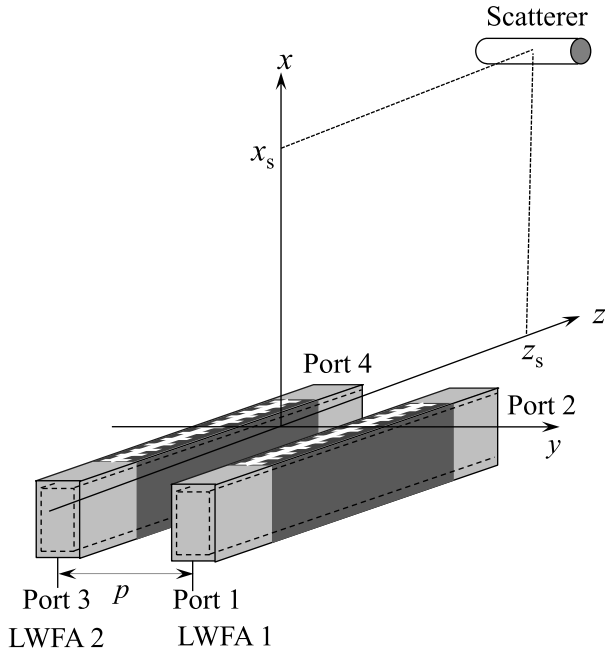


Fig. 10. Experiment setup of the proposed imaging system.

The pitch between the two LWFAs is denoted as p and was set as $p = 30$ mm (with the two antennas in contact) and $p = 50$ mm (which corresponds to a separation between the two antennas of about 2λ for $f = f_c$) to observe the effect of mutual coupling between the two LWFAs. These two scenarios were compared by experiment; a single conducting cylinder of radius $r = 5$ mm and length $l = 50$ mm was used as a scattering object and was positioned at $T(x_{\text{obj}}, z_{\text{obj}}) = (195, 150)$ mm; and the results are shown in Fig. 11. From the figure, the peak due to the object with $p = 50$ mm is clearer than in the case with $p = 30$ mm, which is attributed to be due to the reduced mutual coupling in the $p = 50$ mm case.

To obtain the scattered field by experiment and, thereby, improve the image quality, the S-parameters measured in the

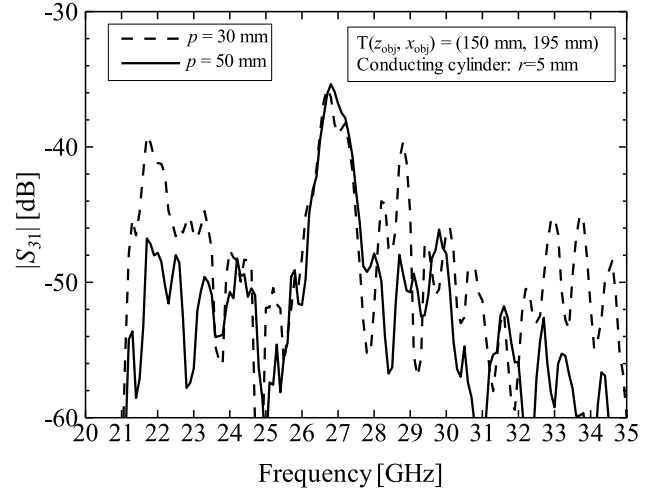


Fig. 11. Measured transmission coefficient in the bistatic case S_{31} with pitch $p = 30$ mm and $p = 50$ mm.

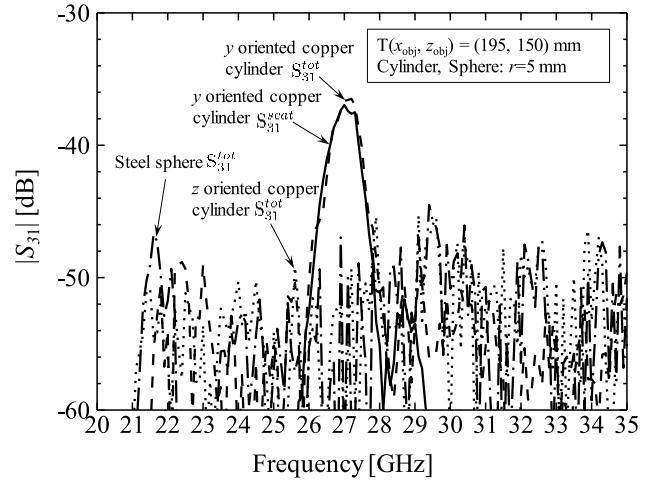


Fig. 12. Measured transmission coefficient in bistatic case with object present, S_{31}^{tot} , and after subtraction of incident field using (11), S_{31}^{scat} .

incident-field case can be subtracted from the total field case by

$$S_{ji}^{\text{scat}} = S_{ji}^{\text{tot}} - S_{ji}^{\text{inc}} \quad (11)$$

where S_{ji}^{tot} is obtained with the scattering object present and S_{ji}^{inc} is obtained without the object present. Equation (11) can be used to eliminate the effect of scattering from the surrounding environment and the effect of mutual coupling between the two antennas.

The transmission coefficient measurements S_{31}^{tot} and S_{31}^{inc} were obtained for the $p = 50$ mm case, S_{31}^{scat} was obtained using (11), and the result is presented in Fig. 12. From the figure, the peak due to the y -oriented copper cylinder object is clearer in the S_{31}^{scat} case than in the S_{31}^{tot} case as the effects of scattering from the surrounding environment and mutual coupling between the two LWFAs have been eliminated by this method. In the case of the z -oriented copper cylinder, a peak could not be observed in Fig. 12 because maximum

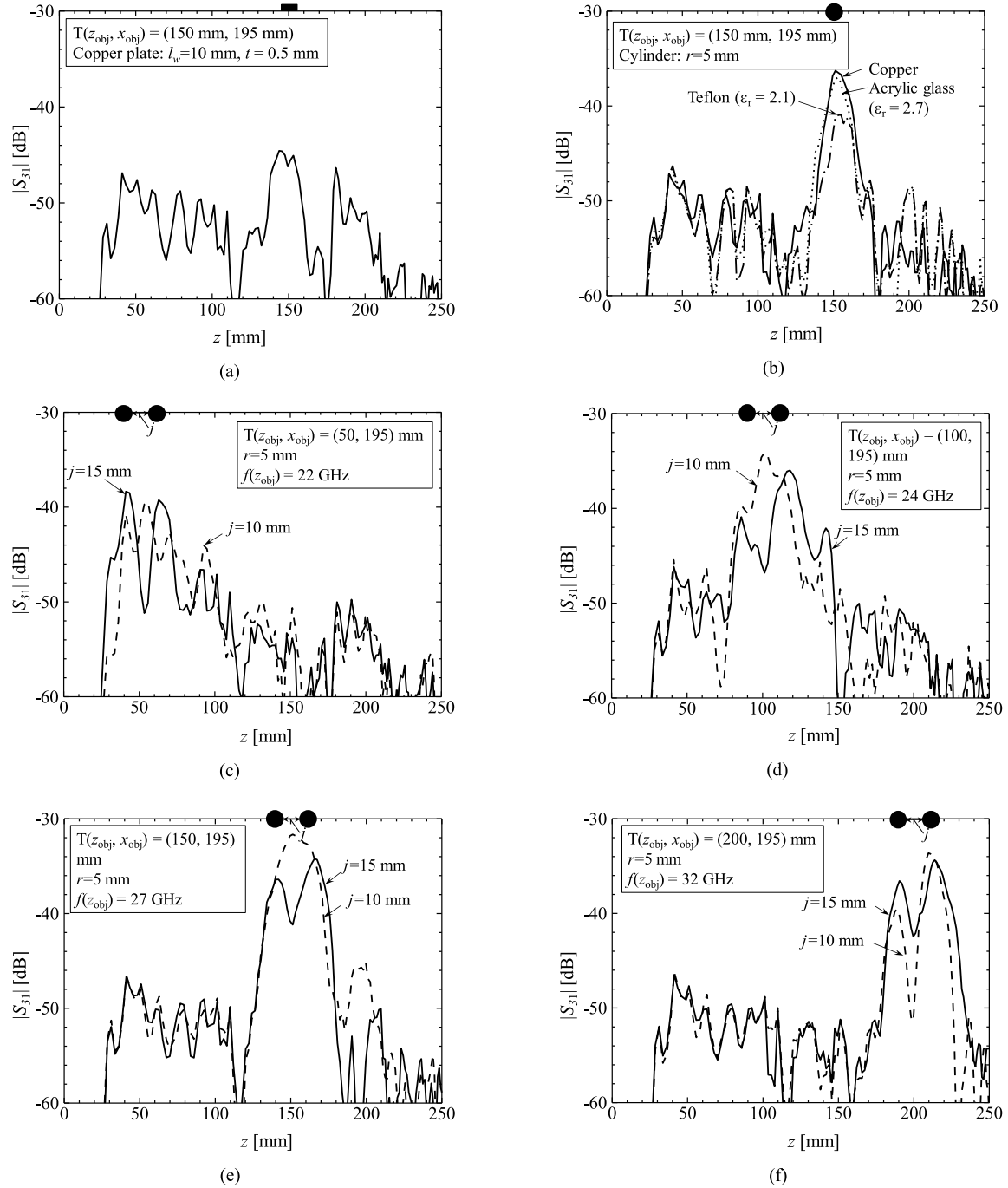


Fig. 15. Transmission coefficient in bistatic case S_{31} with (a) conducting plate, (b) conducting, acrylic glass, and Teflon cylinders positioned at $T(z_{\text{obj}}, x_{\text{obj}}) = (150, 195)$ mm, two conducting cylinders positioned at (c) $z_{\text{obj}} = 50$, (d) $z_{\text{obj}} = 100$, (e) $z_{\text{obj}} = 150$, and (f) $z_{\text{obj}} = 200$ with gaps $j = 10$ mm and $j = 15$ mm and with $p = 50$ mm.

B. 1-D Detection and Resolution

The 1-D detection of both conducting and dielectric objects was performed using the imaging setup shown in Fig. 10. The canonical cylinder and plate objects of radius $r = 5$ mm, width $l_w = 10$ mm, and thickness $t = 0.5$ mm, respectively, were used as scattering objects. Both objects were of length $l = 50$ mm, and (10) was applied to convert the data to the spatial domain.

The first case is that of a conducting cylinder and plate positioned at $T(x_{\text{obj}}, z_{\text{obj}}) = (195, 150)$. S_{31} was measured

in the experiment, and the results are shown in Fig. 15. The peak in the case of the plate in Fig. 15(a) was observed to be lower than in the case of the cylinder shown in Fig. 15(b), and this is expected as the plate reflects the incident field from the LWFA pair compared to the cylinder that has a more uniform scattering pattern in all directions [27], [28]. Due to the inclined nature of the radiation from the LWFA, it is expected that the system would detect plates with l_w less than the resolution of the LWFA as some of the scattering from the edge would be detected by the receiving LWFA, leading to

the observed peak, whereas, for wider l_w , most of the incident field would be reflected away, and in that case, a peak would not be detected.

The next step was then to confirm the detection of dielectric objects, and in this case, acrylic ($\epsilon_r = 2.1$) and Teflon ($\epsilon_r = 2.7$) material dielectric cylinders of the same radius and length as the conducting cylinder were used as the scattering objects. The results from these when positioned at S are shown in Fig. 15(b). The conducting cylinder exhibits the highest peak, followed by the acrylic cylinder and, finally, the Teflon cylinder. The explanation for this phenomenon is that the conducting cylinder, having the highest radar cross section (RCS) of the three materials, scatters a greater proportion of the incident field compared to the other two materials. Acrylic exhibits a higher peak than Teflon because acrylic has a higher ϵ_r than Teflon, which results in a higher RCS relative to the Teflon cylinder case [27]–[29].

The final step was the detection of two conducting cylinders to determine the resolution of the proposed imaging system. Using the equation on spatial resolution based on diffraction from a slit aperture to satisfy the Rayleigh criterion [30], the resolution of the proposed system along the z -direction, as shown in Fig. 14, may be expressed as

$$\Delta z(z_{\text{obj}}) = \frac{R\lambda(z_{\text{obj}})}{L} \quad (12)$$

where $\lambda(z_{\text{obj}})$ is the wavelength of the frequency corresponding to the object position along the z -direction, z_{obj} . L is the length of the antenna, and R is the distance from O to S. The 3 dB width at the focal uw plane along the w -direction, Δw , may then be approximated by

$$\Delta w = \sin\theta_S \Delta z(z_{\text{obj}}) \quad (13)$$

where θ_S is the radiation direction along the diagonal axis from O to S.

Equation (13) can therefore be used to approximate the true resolution of the proposed system at the focal uw plane. Equation (13) can also be used to give some guidance on the heights at which the proposed system can separately detect two objects as Δw can be considered the diameter of the focusing spot of the LWFA [31], [32]. If the two objects are positioned higher or lower than the $\Delta w/2$ around the focusing position $S(x_s, z_s)$ at a given frequency, then it is expected that they cannot be separately detected.

Due to the change in frequency, the resolution is expected to change correspondingly. Therefore, to experimentally determine the resolution, two cylinders were positioned with their centers at $x_{\text{obj}} = 195$ mm and $z_{\text{obj}} = 50, 100, 150,$ and 200 mm, which corresponds to 22, 24, 27, and 32 GHz, respectively, in the frequency domain. The results of (13) at these positions are 13.3, 12.2, 10.8, and 9.1 mm, respectively. To test these values, the cylinders were set with gaps j of 10 and 15 mm between them. From Fig. 15(c) to (f), a single peak was observed with $j = 10$ mm for the 22, 24, and 27 GHz cases, whereas two peaks were observed for $j = 15$ mm. For the 32 GHz case, two peaks were observed for both $j = 10$ mm and $j = 15$ mm, which lends credence to the result of (13).

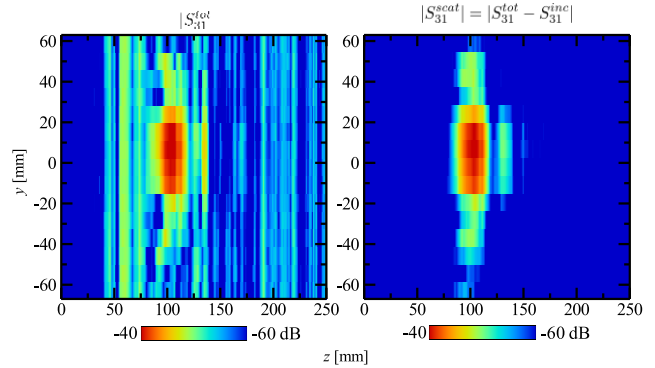


Fig. 16. 2-D image of conducting cylinder generated from measured transmission coefficient in the bistatic case S_{31} at different positions y_{obj} along the y -direction, $x = 195$ mm, and $z = 100$ mm before and after subtraction of the incident field using (11).

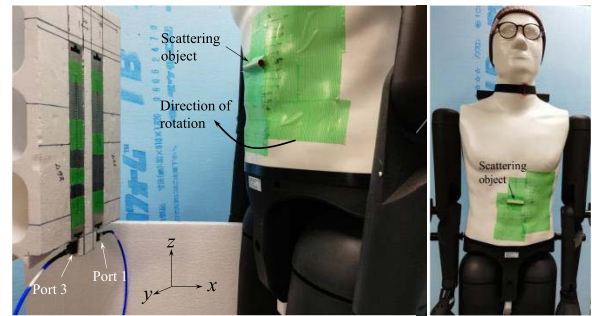
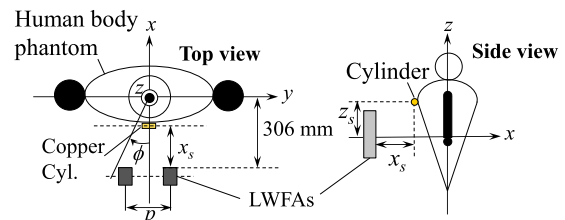


Fig. 17. Experiment setup with the human body phantom.

C. 2-D Imaging

Having confirmed that both conducting and dielectric objects can be detected by the proposed imaging system, the next step was to create 2-D images of the objects. This process was performed using the experimental setup shown in Fig. 10. In this setup, the object was positioned at $x = 195$ mm and $z = 100$ mm; however, the position was changed in the y -direction in 10 mm increments, and S_{31} was recorded for each position.

The recorded S_{31} was then ordered into a 2-D array, and the 2-D image was generated from this array. To improve the quality of the image (11) was applied to the 2-D array and the 2-D image both before and after this operation is indicated in Fig. 16 for the case of a conducting cylinder.

To simulate a practical application case of the proposed imaging system in personnel scanning, the experimental setup shown in Fig. 17 was used. In this setup, the cylindrical objects with $r = 5$ mm and $l = 50$ mm were positioned at $x_s = 195$ mm and $z_s = 150$ mm in front of the human body phantom. The body phantom is the POPEYE10 by SPEAG

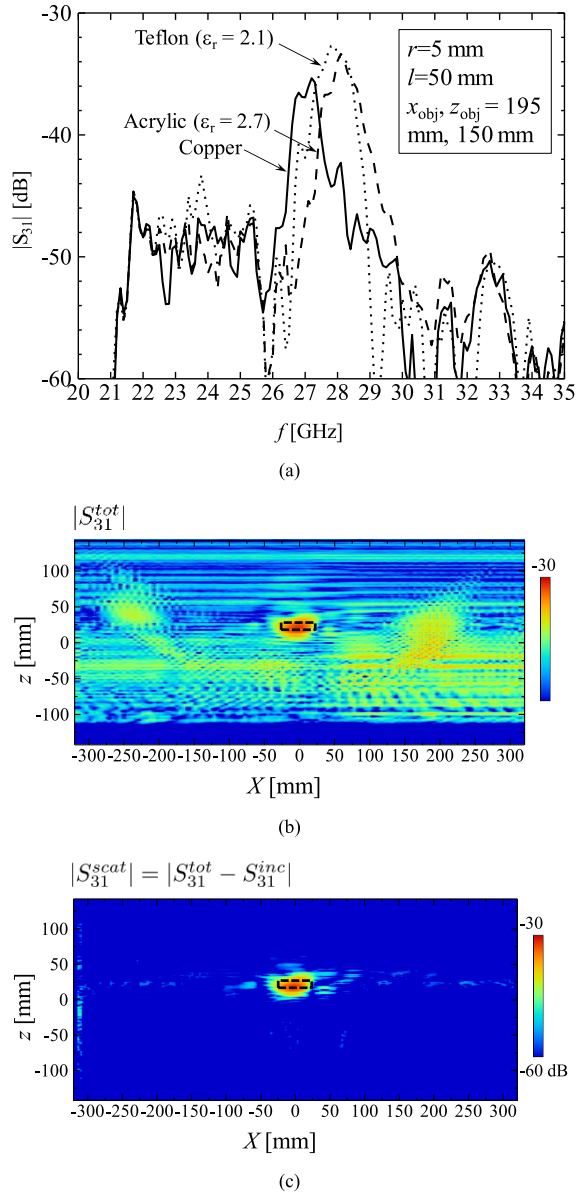


Fig. 18. Transmission coefficient in bistatic case S_{31} with (a) conducting and dielectric cylinders of radius $r = 5$ mm and 2-D image of conducting cylinder generated from measured transmission coefficient in bistatic case at different angles f which has been converted to arc length X with (b) object present, S_{31}^{tot} , and (c) after subtraction of incident field using (11), S_{31}^{scat} .

with similar dielectric properties (within 0.3–100 GHz) and physical characteristics to the human body. First, the 1-D measurements were obtained at $\varphi = 0$, and the results are shown in Fig. 18(a).

From the figure, the case with Teflon ($\epsilon_r = 2.1$) cylinder had the greatest peak, followed by acrylic ($\epsilon_r = 2.7$), and, finally, copper cylinder with the lowest peak. The dielectric cylinders have higher peaks than the conducting cylinder because some of the incident electric fields is transmitted through the dielectric cylinders to the underlying body phantom surface and scattered again, back through the cylinders to the LWFA pair leading to the observed phenomenon. As Teflon has the lower dielectric constant compared to acrylic, a greater proportion of the incident electric field is transmitted through the cylinder through to the surface of the body phantom underneath the

cylinder and scattered back to the LWFA pair compared to the acrylic cylinder, which explains why Teflon has the highest peak.

The 2-D data in the case of the copper cylinder were then generated by rotating the body phantom in the range $-60^\circ \leq \varphi \leq 60^\circ$ and the $|S_{31}|$ measured at each φ at 1° intervals. The measured data were then ordered into a 2-D matrix, f is converted to z , φ is converted to arc length X , and the result is shown in Fig. 18(b). The strong signals on both sides of the actual object position, indicated by the black dashed lines, are caused by the arms of the body phantom, which comes into close proximity with the LWFAs during the rotation. The effect of the human body phantom, the surrounding environment, and the mutual coupling between the LWFAs can be eliminated by using (11) and obtaining the 2-D S_{31}^{scat} similar to the case of the object in free space, and the result is shown in Fig. 18(c), where only the strong scattering corresponding to the object position may be observed. As a peak was observed from Fig. 18(a), a similar 2-D image can be generated for both Teflon and acrylic cylinders following the same procedure.

V. CONCLUSION

An active MMW imaging system based on an LWFA portable enough to be held by hand has been presented in this article. Scanning in one direction is achieved by the frequency scanning characteristic of the antenna, whereas scanning in the second direction would be achieved by the physical movement of the system. The canonical cylinder, spherical, and plate objects were used to determine the effectiveness of the proposed imaging system. First, 1-D detection of conducting and dielectric cylinder and conducting spherical and plate objects was performed. The S-parameter between the input ports of two of the proposed antennas was measured and used to determine the magnitude of the scattered field, and this method was used to locate the object in 1-D.

2-D images were generated by holding the antenna pair stationary and moving the object in one direction. The 1-D data were recorded for each position of the object and combined into a 2-D array, which was used to generate the 2-D image of the object. Also, 2-D data without the object present were subtracted from 2-D data with the object present to improve the image quality by eliminating the effect of the surrounding environment and mutual coupling between the antennas. Similar positions and sizes between the image and the actual object were observed. Finally, the 1-D detection of conducting and dielectric cylinders of the same size positioned in front of a human body phantom with similar dielectric and physical characteristics as the human body was performed. The body phantom was then rotated with the 1-D data recorded at each angle in the case of a conducting cylinder after which a 2-D image was generated from the collected data.

A limitation of the proposed system is that measurements need to be taken twice to improve image quality, and a wideband frequency range is required. In addition, only angle-independent objects oriented along the same direction as the polarization of the LWFAs can be clearly detected, whereas angle-dependent objects, such as planar-shaped objects, will also not be detected unless they are smaller than the resolution

of the proposed system. Therefore, future work would build upon this study to develop methods of overcoming these limitations.

REFERENCES

- [1] L. Yujiri, M. Shoucri, and P. Moffa, "Passive millimeter wave imaging," *IEEE Microw. Mag.*, vol. 4, no. 3, pp. 39–50, Sep. 2003.
- [2] D. M. Sheen *et al.*, "Wide-bandwidth, wide-beamwidth, high-resolution, millimeter-wave imaging for concealed weapon detection," *Proc. SPIE*, vol. 8715, May 2013, Art. no. 871509.
- [3] S. S. Ahmed, "Advanced fully-electronic personnel security screening technology," in *Proc. 9th Eur. Conf. Antennas Propag. (EuCAP)*, 2015, pp. 1–4.
- [4] D. Vizard and R. Doyle, "Invited paper: Advances in millimeter wave imaging and radar systems for civil applications," in *IEEE MTT-S Int. Microw. Symp. Dig.*, Jun. 2006, pp. 94–97.
- [5] J. E. Bjarnason, T. L. J. Chan, A. W. M. Lee, M. A. Celis, and E. R. Brown, "Millimeter-wave, terahertz, and mid-infrared transmission through common clothing," *Appl. Phys. Lett.*, vol. 85, no. 4, pp. 519–521, Apr. 2004.
- [6] Y.-K. Zhu, M.-H. Yang, L. Wu, Y. Sun, and X.-W. Sun, "Millimeter-wave holographic imaging algorithm with amplitude corrections," *Prog. Electromagn. Res. M*, vol. 49, pp. 33–39, 2016.
- [7] D. M. Sheen, D. L. McMakin, and T. E. Hall, "Three-dimensional millimeter-wave imaging for concealed weapon detection," *IEEE Trans. Microw. Theory Techn.*, vol. 49, no. 9, pp. 1581–1592, Sep. 2001.
- [8] S. Vakalis, L. Gong, Y. He, J. Papapolymerou, and J. A. Nazer, "Experimental demonstration and calibration of a 16-element active incoherent millimeter-wave imaging array," *IEEE Trans. Microw. Theory Techn.*, vol. 68, no. 9, pp. 3804–3813, Sep. 2020.
- [9] W. Fang, P. Fei, F. Nian, Y. Yang, and K. Feng, "Ka-band dielectric waveguide antenna array for millimeter wave active imaging system," *J. Infr., Millim., THz Waves*, vol. 35, no. 11, pp. 962–973, Nov. 2014.
- [10] H. Sato *et al.*, "Passive millimeter-wave imaging for security and safety applications," *Proc. SPIE*, vol. 7671, Apr. 2010, Art. no. 76710V.
- [11] D. A. Andrews, S. W. Harmer, N. J. Bowring, N. D. Rezgui, and M. J. Southgate, "Active millimeter wave sensor for standoff concealed threat detection," *IEEE Sensors J.*, vol. 13, no. 12, pp. 4948–4954, Dec. 2013.
- [12] D. R. Jackson, C. Caloz, and T. Itoh, "Leaky-wave antennas," *Proc. IEEE*, vol. 100, no. 7, pp. 2194–2206, Jul. 2012.
- [13] L. O. Goldstone and A. A. Oliner, "Leaky-wave antennas I: Rectangular waveguides," *IRE Trans. Antennas Propag.*, vol. 7, no. 4, pp. 307–319, 1959.
- [14] A. Neto, S. Bruni, G. Gerini, and M. Sabbadini, "The leaky lens: A broad-band fixed-beam leaky-wave antenna," *IEEE Trans. Antennas Propag.*, vol. 53, no. 10, pp. 3240–3246, Oct. 2005.
- [15] C. Pfeiffer and A. Grbic, "Planar lens antennas of subwavelength thickness: Collimating leaky-waves with metasurfaces," *IEEE Trans. Antennas Propag.*, vol. 63, no. 7, pp. 3248–3253, Jul. 2015.
- [16] Y. F. Wu, Y. J. Cheng, and Z. X. Huang, "Ka-band near-field-focused 2-D steering antenna array with a focused Rotman lens," *IEEE Trans. Antennas Propag.*, vol. 66, no. 10, pp. 5204–5213, Oct. 2018.
- [17] Y. F. Wu and Y. J. Cheng, "Two-dimensional near-field focusing folded reversely fed leaky-wave antenna array with high radiation efficiency," *IEEE Trans. Antennas Propag.*, vol. 67, no. 7, pp. 4560–4569, Jul. 2019.
- [18] T. Hashimoto, H. Sato, and Q. Chen, "X-band near-field focusing leaky-wave antenna with inhomogeneous waveguide," in *Proc. 12th Global Symp. Millim. Waves (GSMM)*, May 2019, pp. 72–74.
- [19] T. Hashimoto, H. Sato, and Q. Chen, "Near-field leaky-wave focusing antenna with inhomogeneous rectangular waveguide," *IEICE Commun. Exp.*, vol. 9, no. 6, pp. 1–6, Jun. 2020.
- [20] H. Sato, K. K. Mutai, T. Hashimoto, and Q. Chen, "Near field leaky-wave focusing antenna using inhomogeneous rectangular waveguide," in *Proc. Int. Symp. Antennas Propag. (ISAP)*, Jan. 2021, pp. 19–20.
- [21] P. Burghignoli, F. Frezza, A. Galli, and G. Schettini, "Synthesis of broad-beam patterns through leaky-wave antennas with rectilinear geometry," *IEEE Antennas Wireless Propag. Lett.*, vol. 2, pp. 136–139, 2003.
- [22] C. H. Walter, "Traveling wave antenna design," in *Traveling Wave Antennas*, 1st ed. New York, NY, USA: MHP, 1965, ch. 4, sec. 3, p. 155.
- [23] T. R. Cameron, A. T. Sutinjo, and M. Okoniewski, "Analysis and design of slitted waveguides with suppressed slot-mode using periodic FDTD," *IEEE Trans. Antennas Propag.*, vol. 60, no. 8, pp. 3654–3660, Aug. 2012.
- [24] T. Kokkinos, C. D. Sarris, and G. V. Eleftheriades, "Periodic FDTD analysis of leaky-wave structures and applications to the analysis of negative-refractive-index leaky-wave antennas," *IEEE Trans. Microw. Theory Techn.*, vol. 54, no. 4, pp. 1619–1630, Jun. 2006.
- [25] A. Sutinjo, M. Okoniewski, and R. H. Johnston, "Suppression of the slot-mode radiation in a slitted waveguide using periodic slot perturbations," *IEEE Antennas Wireless Propag. Lett.*, vol. 8, pp. 550–553, 2009.
- [26] K. K. Mutai, H. Sato, and Q. Chen, "Development of an active millimeter wave imaging system using leaky-wave focusing antenna," in *Proc. Int. Conf. Emerg. Technol. Commun. (ICETC)*, Dec. 2020.
- [27] C. A. Balanis, "Scattering," in *Advanced Engineering Electromagnetics*, 2nd ed. New York, NY, USA: JW&B, 2012, pp. 575–668.
- [28] G. T. Ruck, D. E. Barrick, W. D. Stuart, and C. K. Krichbaum, *Radar Cross Section Handbook*, vol. 1, 1st ed. New York, NY, USA: Plenum, 1970.
- [29] K. Umashankar and A. Taflove, "A novel method to analyze electromagnetic scattering of complex objects," *IEEE Trans. Electromagn. Compat.*, vol. EMC-24, no. 4, pp. 397–405, Nov. 1982.
- [30] G. R. Fowles, "Diffraction," in *Introduction to Modern Optics*, 1st ed. New York, NY, USA: HRW, 1968, ch. 4, sec. 4, pp. 114–125.
- [31] A. Buffi, P. Nepa, and G. Manara, "Design criteria for near-field-focused planar arrays," *IEEE Antennas Propag. Mag.*, vol. 54, no. 1, pp. 40–50, Feb. 2012.
- [32] J. Sherman, "Properties of focused apertures in the Fresnel region," *IRE Trans. Antennas Propag.*, vol. 10, no. 4, pp. 399–408, 1962.



Kevin Kipruto Mutai (Graduate Student Member, IEEE) received the B.E. degrees from the Jomo Kenyatta University of Agriculture and Technology (JKUAT), Nairobi, Kenya, in 2017 and 2018. He is currently pursuing the M.E. degree with the Department of Communications Engineering, Tohoku University, Sendai, Japan.

His current research interests include leaky-wave antennas, active/passive millimeter-wave imaging, computational electromagnetics, antenna arrays, and aperture antennas.



Hiroyasu Sato (Member, IEEE) received the B.E. and M.E. degrees from Chuo University, Tokyo, Japan, in 1993 and 1995, respectively, and the D.E. degree from Tohoku University, Sendai, Japan, in 1998.

He is currently an Assistant Professor with the Department of Communications Engineering, Tohoku University. His current research interests include the experimental study of electromagnetic waves, computational electromagnetics, antennas in plasma, antennas for plasma production, broad-band antennas, wireless power transfer, and active/passive millimeter-wave imaging.

Dr. Sato is also a member of the Institute of Electronics, Information and Communication Engineers (IEICE). He received the First Place of the Best Paper Award from the International Symposium on Antennas and Propagation (ISAP) in 2017.

Dr. Sato is also a member of the Institute of Electronics, Information and Communication Engineers (IEICE). He received the First Place of the Best Paper Award from the International Symposium on Antennas and Propagation (ISAP) in 2017.



Qiang Chen (Senior Member, IEEE) received the B.E. degree from Xidian University, Xi'an, China, in 1986, and the M.E. and D.E. degrees from Tohoku University, Sendai, Japan, in 1991 and 1994, respectively.

He is currently a Chair Professor with the Electromagnetic Engineering Laboratory, Department of Communications Engineering, Faculty of Engineering, Tohoku University. His primary research interests include antennas, microwave and millimeter waves, electromagnetics measurement, and computational electromagnetics.

Dr. Chen is also a fellow of the Institute of Electronics, Information and Communication Engineers (IEICE). He received the Best Paper Award and the Zen-Ichi Kiyasu Award in 2009 from IEICE. He has served as the Chair of the IEICE Technical Committee on Photonics-applied Electromagnetics Measurement from 2012 to 2014, the IEICE Technical Committee on Wireless Power Transfer from 2016 to 2018, and the IEEE Antennas and Propagation Society Tokyo Chapter from 2017 to 2018. He is also the Chair of the IEICE Technical Committee on Antennas and Propagation.